

Isotropic Forming of Porous Structures via Metal Injection Molding

Donald F. Heaney*, John D. Gurosik, and Chantal Binet

The Pennsylvania State University,
Center for Innovative Sintered Products,
118 Research West,
University Park, PA 16802-6809

Submitted to Journal of Materials Science

Thursday, October 09, 2003

* Author to whom all correspondence should be addressed.

ABSTRACT

Porous 316L stainless steel structures have been fabricated via metal injection molding (MIM) for both water- and gas-atomized powders. The metal injection molding process offers the unique ability to produce net-shape parts with homogenous porosity, pore structure, and permeability. In this study, porous MIM structures were analyzed for porosity, pore size, permeability, and thermal conductivity as a function of powder type and processing conditions. A typical MIM powder (<20 μm) processed at 50 volume % loading in a binder system produced a uniform pore structure with a permeability of less than $1 \cdot 10^{-13} \text{ m}^2$ and a maximum pore radius of less than 5 μm . Water-atomized powder proved to be better suited for low-solids-loading metal injection molding (<50vol% loading) since its interparticle friction provided greater strength and fewer defects during the molding and debinding process steps. Measurements of thermal conductivity show that the water-atomized powder had less thermal conductivity ($\sim 2 \text{ W/m-K}$) than the gas-atomized powder ($\sim 3 \text{ W/m-K}$).

Key Words: Porous Structures, Powder Injection Molding, Maximum Pore Size Prediction, Thermal Conductivity Prediction, Binder Assisted Forming.

1. Introduction

Porous metal structures are used in many applications throughout industry. Applications for porous metals include filtering systems, heat transfer systems, self-lubricating bearings, orthopedic joint replacements, catalytic filtering systems, batteries, and wicking devices. All these applications require controlled specimen characteristics and properties – some examples are pore size, permeability, density, thermal conductivity, and surface area. Most applications are currently manufactured using methods that require secondary operations such as machining and etching or using methods that produce gradients in pore size and permeability such as the conventional P/M pressing and sintering process. Many applications such as orthopedics, wicks, and electronics require more uniform pore size throughout the structure and a minimum of secondary operations to preserve the pristine rough surface structure. These uniformity requirements cannot be achieved using standard processing techniques; therefore, non-traditional techniques such as binder-assisted forming are considered.

The purpose of this investigation was to establish a metal injection molding manufacturing method for porous 316L stainless steel structures and to characterize the porous product. The relationship between pore radius, permeability, and thermal conductivity as a function of the powder type and processing conditions was defined.

2. Background

Metal injection molding method of manufacturing net-shape components that is experiencing commercial acceptance [1]. In this process, a metal powder is mixed with an organic binder to produce a mixture, or feedstock, that has a sufficiently low viscosity to be molded using a high-

pressure screw injection-molding machine [2, 3]. Since molded components are typically 30 to 60 volume % polymer, a unique opportunity exists to produce net-shape porous materials by simply removing the binder and sinter-bonding the compact without densification. This becomes more intriguing when considering the relative isotropic nature [4], the limited secondary operations required, and the recyclability of the feedstock for the injection molding process. In addition, the process is more economical and more geometrically precise than other isotropic forming techniques such as cold isostatic pressing.

Early attempts at binder-assisted molding of net-shape porous structures [5] have been reported, but their uses have been limited. Typically, manufacturing methods for porous material consist of compacting a metal powder in a die and subsequently machining and etching to achieve the final geometry. Die compaction is limited not only in its shape-making capabilities due to tooling and compaction constraints, but also in its chance for producing an isotropic pore size, permeability, and density. The product of this technique has high densities in the top and bottom of the sample (near the top and bottom punches) and significantly less density in the middle of the compact. This problem increases as the height to width ratio increases, making long, thin parts hard or impossible to manufacture uniformly. Other fabrication techniques consist of loose powder sintering followed by machining, and a new technique involving selective laser sintering has also been demonstrated [6]. Although the selective laser sintering technique can produce net-shape components, it has limited dimensional precision and its production rate is in the order of hours rather than seconds. Therefore, an ideal opportunity exists for the mass manufacturing of net-shape porous structures with relatively isotropic pore structure by the use of metal injection molding; however, there is no engineering data for this technique.

A review of requirements for different porous applications shows that a large range of porous characteristics are needed [7, 8, 9]. Pore sizes in the 0.5-200 μm range are used in the filter industry, while a pore radius in the 100-500 μm range is important for proper bone ingrowths in joint replacement applications. In heat transfer systems, porous metals have a broad range of pore size, starting at less than 2 μm for capillary metal wick systems to over 200 μm for convection applications. The improvement of porous metal heat transfer is important for several applications, from computer processors to turbines. Batteries also benefit from increasing the surface area and subsequently managing the pore size of materials, resulting in both longer life and improved performance. Thus, advances in the method by which porous materials are fabricated and tailored to a particular need will advance applications to higher levels.

3. Experimental

To evaluate the capability of the MIM process to make porous materials, a design of experiments (DOE) was constructed. The use of a DOE permits suitable raw materials and process parameters to be successfully defined for making porous material. The DOE presented in this paper was constructed using two powder-polymer ratios, two powder types, and two sintering temperatures (Table I). In Table I, atomization refers to the method of powder manufacturing, and powder loading refers to the percentage of powder, on a volume basis, contained in the feedstock. Once the conditions to be used for the DOE were decided, appropriate raw material was characterized and mixed. Feedstocks were subsequently prepared and 10 samples of each condition were molded. The as-molded MIM samples were solvent and thermal debound prior to sintering. The samples were then sintered to the temperature chosen in the DOE. These low

sintering temperatures were chosen to bring the components to temperatures that could promote an initial stage of sintering where neck formation between particles is started without densification. Finally, the 10 samples of each condition were characterized by measuring their porosity, pore size, permeability, and thermal conductivity. All values had approximately a $\pm 5\%$ range in measurement, except for the thermal conductivity, which had approximately $\pm 8\%$ range in measurement.

3.1 Powder and binder characterization

Two 316L stainless steel powder types (water and gas atomized) were used to make porous material and the characteristics of each were evaluated. Particle size distribution, tap density, and theoretical density were characterized. Theoretical density was measured using a helium pycnometer, which measures the density of a powder by calculating the ratio between its measured mass and the difference between the known volume of a container filled with helium and the volume of the same container filled with powder and helium. Tap density was measured via MPIF Standard 46 test method [10]. This measurement evaluates the highest density that can be achieved by vibrating a powder. It gives an indication of the amount of powder that can be loaded into a polymer and of how well the powders pack together. Three measurements of tap and theoretical densities were taken for each powder.

Particle size distribution was measured three times for each powder using a laser light scattering technique on a Horiba LA 920. Typically, three points of powder size values, designated as D_{10} , D_{50} and D_{90} , are used to characterize the powders; the subscript indicates the percentage of particles that are smaller than the measured value.

Average values of the densities and particle size distribution are reported in Table II, along with oxygen level. The oxygen content was taken from the vendor certification. Oxygen content in powder influences the sintering potential. Higher oxygen content signifies a thicker oxide layer on the surface thus reducing the rate of powder sintering for higher oxide content powders. Scanning Electron Microscopy (SEM) was used to characterize the shape of powder samples (Fig. 1 and 2). The gas-atomized powder is mostly spherical, while the water-atomized powder is irregular.

3.2 Feedstock preparation and molding

Once the particle characteristics were determined, the feedstocks were prepared by dry mixing a wax/polymer binder system (Parrafin Wax 7355 from Dussek Campbell and Pro-Flow 3000 from PolyVisions) with each of the powders at the designed powder loading. The feedstocks were then mixed at 160°C using a sigma blade mixer. Cylindrical specimens with a diameter and length of 1.27 cm were molded using a 30-ton injection-molding machine. Molding parameters consisted of a melt temperature of 160°C, a mold temperature of 30°C, an injection speed of 30 cm³/sec, and a hold pressure of 50 MPa for 6 sec.

3.3 Debinding and Sintering

After molding, the specimens were solvent debound in heptane to remove the wax portion of the binder system. A solvent debinding temperature of 40°C was used to eliminate distortion problems that were observed at 60°C, particularly for the samples made with the gas-atomized powders. The low solids loading of these formulations caused this distortion since higher solids

loading of the same material shows no distortion in 60°C heptanes. After solvent debinding, thermal debinding was performed at temperatures of 200-500°C in flowing hydrogen gas. Due to the uncharacteristically low powder loading (<50 vol %) inherent in these formulations, the specimens were packed in fine 10µm, A11 alumina powder from Alcoa to provide structural support and binder wicking during the burnout process. Once the binder was burnt out, the samples were sintered at either 850°C or 950°C for one hour in flowing hydrogen gas.

3.4 Porosity, permeability and maximum pore radius

After sintering, the defect-free components were measured to ascertain the porosity, permeability, pore radius, and thermal conductivity. The porosity (ϵ) of the samples was calculated as follows:

$$\epsilon = 1 - \frac{\rho_{\text{geometric}}}{\rho_{\text{theoretical}}} \quad (1)$$

The $\rho_{\text{geometric}}$ is simply the mass divided by volume for the processed sample. The theoretical density, as is shown for each powder in Table II, was determined using a pycnometer. The permeability was measured using Darcy's Law. Cylindrical samples were placed in the flow path of acetone. The pressure drop across the sample was measured and used to calculate permeability K (m^2) as follows [11]:

$$K = \frac{QL\eta}{\Delta PA} \quad (2)$$

where Q is the solvent flow rate (m³/sec), L is the sample length (m), η is the viscosity of acetone (0.306 mPa·s [12]), ΔP is the pressure drop across the sample (Pa), and A is the cross-sectional area of the sample (m²).

The maximum pore radius was calculated by immersing the porous material in acetone and applying air pressure until the first bubbles of air appeared. The maximum pore radius (r_c) was calculated from the surface tension of the acetone on the stainless steel ($\sigma=23.46$ mN/m [12]) and the pressure difference (Δp) as follows:

$$r_c = \frac{2\sigma}{\Delta p} \quad (3)$$

3.5 Thermal Conductivity

Thermal conductivity was determined using a version of the apparatus described by Francl and Kingery [13]. In this method, the sample to be tested is sandwiched between two materials of known thermal conductivity and thermocouples located on both ends of the sample, and the references are used to measure temperature differences as heat flows from a heat source to a heat sink. This is a comparative method, which permits us to extract thermal conductivity with the following equations [13]:

$$q = \frac{k_1 A_1 \Delta t_1}{\Delta l_1} = \frac{k_2 A_2 \Delta t_2}{\Delta l_2} = \frac{k_3 A_3 \Delta t_3}{\Delta l_3} \quad (4)$$

$$k_2 = k_1 \cdot \frac{A_1}{A_2} \cdot \frac{\Delta t_1}{\Delta t_2} \cdot \frac{\Delta l_1}{\Delta l_2} = k_3 \cdot \frac{A_3}{A_2} \cdot \frac{\Delta t_3}{\Delta t_2} \cdot \frac{\Delta l_3}{\Delta l_2} \quad (5)$$

where q is the heat flow, k is the thermal conductivity, A is the mean area, Δt is the temperature difference between thermocouples, and Δl is the distance between the thermocouples. The subscripts indicate the two references with known thermal conductivity (1 and 3) and the sample (2).

4. Results

Table III presents pictures of the samples after sintering and summarizes the observations noted for each of the conditions of Table I. Four of the DOE conditions showed major defects.

Conditions 1 and 2, which were both water-atomized powder sintered at 850°C, showed no handling strength after sintering. Conditions 5 and 7, which were both gas-atomized powder with 40 vol% powder loading, showed defects such as cracks and blistering. These four conditions were not used for further characterization and measurements since they would be useless for any application. The samples from the four remaining conditions kept their shape but experienced some shrinkage compared to the mold dimension (diameter = 1.27 cm). The samples made with the water-atomized powder with 50 vol % powder-loading showed an average 3.5% of linear shrinkage, while the samples made with the same powder but loaded with only 40 vol% powder loading shrank on average 7.6%. The samples made with the gas-atomized powder showed average shrinkage of 10%.

SEM of the microstructure of the samples was performed after sintering for Conditions 4 and 8. The samples were mounted with an epoxy infiltration technique that permits one to view the porosity without damaging the lightly bounded powder during polishing. Fig. 3 shows the

microstructure of a sample made with the water-atomized powder and Fig. 4 shows one made with the gas-atomized powder. Both pictures were taken for samples with 50 vol % powder loading and sintered at 950°C.

Porosity, pore radius, permeability and thermal conductivity were measured on the samples of conditions 3, 4, 6, and 8. Table IV summarizes the average of measurements taken on three samples of each condition. As should be expected, an increase in sintering temperature (Condition 6 vs 8), with other variables held constant, resulted in a smaller pore radius and lower permeability. This was observed only for the samples made from gas-atomized powder since the samples made from water-atomized powder were eliminated from the experiment at this lower sintering temperature due to poor sintering. Lowering the powder loading, with other variables constant, resulted in a larger pore radius and a higher permeability, which was also to be expected. This was performed only on the samples made from water-atomized powder, since the samples made from gas-atomized powder could be processed only at the higher powder loading. A head-to-head comparison between the two powders showed that the thermal conductivity is lower for the water-atomized powder and that the pore size, permeability, and porosity are all smaller for the gas-atomized powder.

5. Discussion

5.1 DOE conditions

Of all the samples tested in the DOE, the low sintering temperature (850°C), water-atomized conditions (1 and 2) were eliminated since they offered no handling strength for testing and would prove useless for any application. The insufficient sintering of these two conditions could

be the result of the larger particle size of the water-atomized powder or its higher oxygen content compared to the gas-atomized powder. Conditions 5 and 7, which are the gas-atomized conditions at low solids loading, were also eliminated since they were more susceptible to defects such as cracking and blistering during the process. The defects observed in these two cases can be attributed to the spherical shape of the powder, its low interparticle friction, and its subsequent low strength during binder removal. The irregular shape that is characteristic of water-atomized powders provided interparticle friction and interlocking, which proved useful in limiting distortion and defect generation during the solvent and thermal debinding processes.

The conditions that gave the best results for shape retention and handling strength are Conditions 4 and 8. Condition 4 has a higher powder loading and the highest sintering temperature used with the water-atomized powder. This condition shows better results for shape retention than the one with a lowest powder loading (Condition 3), although this one was acceptable. The highest powder loading made the sintering easier and helped to keep the shape, since the contact between particles is higher than with a lower powder loading. Condition 8 had the highest powder loading and sintering temperature of the samples made with gas-atomized powder.

In general, the water-atomized powder is better suited for the low solid loading condition.

Again, its irregular shaped particles promote interparticle friction that causes them to interlock, offering strengthening.

5.2 Porosity

The porosity measured for the gas-atomized powder is lower than the porosity measured for the water-atomized powder, while the thermal conductivity is higher for the gas-atomized powder. This should be expected since the sintering activity of the gas-atomized powders is higher due to their reduced level of oxidation and smaller particle size.

Porosity of 40 to 55%, pore radius of 4-10 μm , permeability in the 10^{-14} m^2 range, and thermal conductivity of 1.5 to 3 W/(m-K) are typical for structures prepared using $<20\mu\text{m}$ 316L stainless steel powders. However, these values are not suitable for all applications. For example, pore sizes for wicking need to be approximately 2 μm and those for bone ingrowths need to be on the order of 100-500 μm . Therefore, a theoretical model to predict pore sizes was reviewed to validate our findings and predict future efforts. Consider Kozeny's equation for the relationship between average pore size (\bar{D}), particle size (a), and porosity (ϵ) [14, 15].

$$\bar{D} = \frac{2}{3} \left(\frac{\epsilon}{1-\epsilon} \right) a \quad (6)$$

According to this equation, the pore size will increase with an increase in porosity and powder size. The porosity and powder size are both smaller for the gas-atomized powders than for the water-atomized powder, thus the former have smaller maximum pore size.

This equation was used to predict theoretical pore sizes using the values of D_{10} , D_{50} , and D_{90} from the powder size distribution of the two powders as the "a" value in Equation 6. These predicted maximum pore sizes were compared to the measured maximum pore sizes, and their

respective values are shown in Table V and illustrated in a chart in Fig. 5. The measured maximum pore radius values are best predicted using powder sizes between the D_{50} and D_{90} of the powder size distribution. Using this method, the values are more closely approximated by the D_{50} for the water-atomized powder and by the D_{90} for the gas-atomized powder.

The D_{50} is more favorable for predicting the maximum pore size for the water-atomized powders and the D_{90} is more favorable for predicting the maximum pore size for the gas-atomized powders due to the difference in the powder geometry. Belov *et al.* [14] suggest that as the particle shape passes from spherical to random-shaped, the relative pore size should decrease. Thus, the observations here validate this suggestion. Consider that the D_{90} powder size of the spherical powder predicts the maximum pore size while the smaller D_{50} size of the irregular powder predicts its maximum pore size. As the powder becomes more irregular, smaller sizes of the particle distribution best predict the maximum pore size.

Using this model and the observations made in this paper, to obtain a maximum pore size of 2 μm with a powder loading of 50% and a sintering temperature of 950°C with the water atomized powder, a powder with a D_{50} of 3 μm should be used. For the same powder and condition but a pore size in the range of 100-500 μm , a D_{50} powder size would need to be between 150 and 750 μm .

5.3 Thermal conductivity

Thermal conductivity of porous materials is of high interest for the scientific and engineering community. Therefore, a large number of experimental characterizations and models are

presented in the literature [16-21]. In this paper, experimental results of thermal conductivities are compared with four models from the literature that calculate effective thermal conductivity as a function of porosity [16-21]. A simple and classical equation to evaluate effective thermal conductivity (k_{eff}) of porous material was based on the assumption that the pores were cylindrical [16, 17]:

$$k_{eff} = \frac{k}{k_B} = 1 - \varepsilon \quad (7)$$

where k is the thermal conductivity of the porous material and k_B is the thermal conductivity of the bulk material. This equation was reported to overestimate the thermal conductivity for porous material made by powder metallurgy. Grootenhuis *et al* [18] reported that thermal conductivity of porous bronze is represented by the following equation:

$$k_{eff} = \frac{k}{k_B} = 1 - 2.1 \varepsilon \quad (8)$$

Agapiou and DeVries [19] proposed a linear empirical model based on thermal conductivity measurements of an austenitic 304 stainless steel porous material. Their model is reported here even if it is claimed to be valid only for porosity less than 40 vol % because it was derived for a similar porous alloy. The empirical equation suggested by Agapiou and DeVries [19] for effective thermal conductivity as a function of porosity is:

$$k_{eff} = \frac{k}{k_B} = 0.95 - 1.57\varepsilon \quad (9)$$

Finally, a semi-empirical model was derived by Aivazov and Domashnev [20] to express thermal conductivity of porous materials:

$$k_{eff} = \frac{k}{k_B} = \frac{1 - \varepsilon}{1 + n\varepsilon^2} \quad (10)$$

with “n” being a constant determined experimentally. Koh and Fortini [21] determined the value of n for this model with several measurements of thermal conductivity on three different porous material made by compaction of 304 L stainless steel powder and woven wire, and copper spherical-powder. They found that a value of n = 11 is statistically representative for their experimental results and others from the literature [21].

Using Equations 7 to 10, thermal conductivities were calculated as a function of porosity and reported in Fig. 6. The values measured experimentally, divided by the thermal conductivity of 316L stainless steel (16.2 W/m-K [22]), are also reported.

A considerable difference is observed with the model of Equation 7. As reported before, this model overestimates the effective thermal conductivity. The linear model of Equation 8 predicts thermal conductivity that diverges from the experimental value. It was reported by Koh and Fortini [21] that this correlation better predicts the thermal conductivity for porous material with porosity smaller than 30 vol% and tends to underestimate the conductivity when the porosity is

larger. Experimental conductivity values measured reinforce this statement. The empirical model of Equation 9 is closer to the experimental values than the one of Equation 8. However, this linear model does not follow the curve observed experimentally. Considering that thermal conductivity cannot be less than zero, the linear model proposed by Agapiou and DeVries [19] is not valid at high porosities. The model derived by Aivazov and Domashnev [20] represents well the measurements performed in this paper. Again, the experimental thermal conductivity values confirm that the model of Equation 10 correlates well with the porous stainless steel material made by powder metallurgy.

6. Conclusions

In general, both powders are useful in the manufacture of porous net-shape products by injection molding. The experiments conducted show that metal injection molding is a viable method of creating porous metal structures. Porosity of 40 to 55%, pore radius of 4-10 μm , permeability in the 10^{-14} m^2 range, and thermal conductivity of 1.5 to 3 $\text{W}/(\text{m}\cdot\text{K})$ are typical. The water-atomized powder was better suited to the low powder loading process due to its irregular shape and subsequent robustness during processing. The thermal conductivity is lower for the water-atomized powder and the pore size, permeability, and porosity are all smaller for the gas-atomized powder. Predictive calculations show that values between the D_{50} and D_{90} of the particle size distribution are best for estimating maximum pore sizes. As powder shape moves from spherical to irregular for the same size distribution, the relative pore size decreases. Thermal conductivity of porous material made by an injection molding is quite complex. Microstructure resulting from this process is unique and directly influences the thermal properties. The particle size distribution and the size of the neck that forms during the sintering

step will greatly influence the thermal conductivity values [23]. However, the semi-empirical model derived by Aivazov and Domashnev [19] with $n=11$ as calculated by Koh and Fortini [21] can be used to predict thermal conductivity of porous 316 L stainless steel made by metal injection molding.

References

1. R. M. GERMAN and R. G. CORNWALL, *Metal Powder Report* **56** (2) (2001) 22.
2. R. M. GERMAN and A. BOSE, in “Injection Molding of Metal and Ceramic” (Metal Powder Industries Federation, Princeton, NJ, 1997).
3. H. I. BAKAN, D. F. HEANEY, and R. M. GERMAN, *Journal of Powder Metallurgy* **44** (3) (2001) 235.
4. C. BINET, D. F. HEANEY, J. C. PIEMME, and P. BURKE, in *Advances in Powder Metallurgy and Particulate Materials*, Orlando, FL, June 2002, compiled by V. Arnhold, C-L. Chu, W.F. Jandeska and H. I. Sanderow (Metal Powder Industries Federation, Princeton, NJ, 2002) p. 10-210.
5. J. C. DUDDY, in US patent # 3,266,893, *Method for the Manufacturing Porous Sinterable Articles* (August 16, 1966).
6. D. F. HEANEY and R. M. GERMAN, in *Advances in Powder Metallurgy and Particulate Materials*, New Orleans, La, May 2001, compiled by W. B. Eisen and S. Kassam (Metal Powder Industries Federation, Princeton, NJ, 2001) p. 8-73.
7. Guidance Document For Testing Orthopedic Implants With Modified Metallic Surfaces Apposing Bone or Bone Cement, Orthopedic Devices Branch, Division of General and

Restorative Devices, Office of Device Evaluation, Center for Devices and Radiological Health, U.S. Food and Drug Administration, 1994, April 28, <http://www.fda.gov/cdrh/ode/827.html>

8. G. SRIKANTH, Membrane Separation Processes - Technology and Business Opportunities, <http://www.tifac.org.in/news/memb.htm>

9. R. M. GERMAN, in "Powder Metallurgy Science" (Metal Powder Industries Federation, Princeton, NJ, 1994).

10. MPIF Standard Test Methods, Standard 46, Determination of Tap Density of Metal Powders, issued 1981.

11. R. M. GERMAN, in Advances in Powder Technology, edited by G. Y. Chin (American Society for Metals, Metals Park, OH, 1982) p. 225.

12. D. R. LIDE, in "CRC Handbook of Chemistry and Physics" (CRC Press, Washington, DC, 80th Edition, 1999-2000) p. 6-145 & p. 6-180.

13. J. FRANCL and W. KINGERY, *J. Am. Ceram. Soc.* **37** (2) (1954) 80.

14. S. V. BELOV, O. G. KATUESOV, and V. M. POLYAEV, *Soviet Powder Met. Metal Ceram.*, **11** (1972) 733.

15. S. M. SWEENEY and M. J. MAYO, *J. Am. Ceram. Soc.* **82** (7) (1999) 1931.
16. D.R. POIRIER and G.H. GEIGER, in “Transport Phenomena in Materials Processing” (The Minerals, Metals & Materials Society, Warrendale, PA, 1994) p. 208.
17. E. E. GONZO, *Chemical Engineering Journal*, **90** (2002) 299.
18. P. GROOTENHUIS, R. W. POWELL and R. P. Tye, *Proc. Phys. Soc.* **B65** (1952) 502.
19. J. S. AGAPIOU and M. F. DEVRIES, *J. Heat Transf.*, **111** (1989) 281.
20. M. I. AIVAZOV and I. A. DOMASHNEV, *Poroshkovaya metallurgiya*, **8** (9) (1968) 51.
21. J. C. KOH and A. FORTINI, *Int. J. Heat Mass Transf.*, **16** (1973) 2013.
22. M. BAUCCIO (ed), in “ASM Metals Reference Book, 3rd ed.” (ASM International, Materials Park, OH, 1993) p. 360.
23. A. BIRNBOIM, T. OLORUNYOLEMI, and Y. CARMEL, *J. Am. Ceram. Soc.* **84** (2001) 1315.

Table I. Design of Experiments

Condition	Atomization	Powder Loading (volume %)	Sintering Temperature (°C)
1	Water	40	850
2	Water	50	850
3	Water	40	950
4	Water	50	950
5	Gas	40	850
6	Gas	50	850
7	Gas	40	950
8	Gas	50	950

Table II. Powder Characteristics

Atomization	Avg. Tap Density (g/cc)	Avg. Theoretical Density (g/cc)	D ₁₀ (μm)	D ₅₀ (μm)	D ₉₀ (μm)	Oxygen (wt %)
Water	3.99	7.91	8.2	15.9	29.0	0.38
Gas	4.92	7.93	4.2	10.3	19.3	0.038

Table III. DOE “fallout” as a result of processing defects

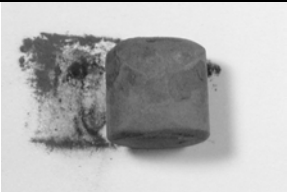
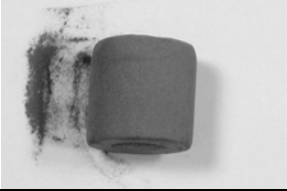
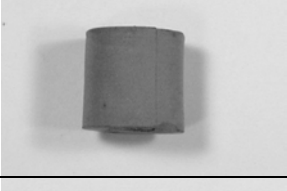
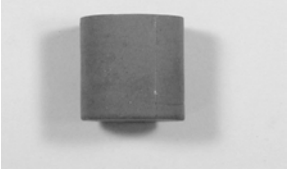
Condition	Linear Shrinkage	Process Observations	
1	Not measured	No Strength	
2	Not measured	No Strength	
3	7.6 %	Good	
4	3.5 %	Good	
5	Not measured	Defects	
6	10 %	Good	
7	Not measured	Defects	
8	10 %	Good	

Table IV. Summary of Results

Condition	Porosity (%) ±5%	Maximum Pore Radius, r_p (μm) ±5%	Permeability, K (m^2) ±5%	Thermal Conductivity, k (W/m-K) ±8%
3	54.8	7.3	$1.4 \cdot 10^{-13}$	1.8
4	49.2	5.2	$9.0 \cdot 10^{-14}$	2.0
6	46.1	4.4	$6.7 \cdot 10^{-14}$	2.4
8	41.0	4.1	$4.1 \cdot 10^{-14}$	2.9

Table V. Calculated Pore Radii for Different Powder Sizes Compared to Measured Maximum

Pore Radii

Powder type	Water		Gas	
	Measured Porosity (%)	54.8	49.2	46.1
D ₁₀ powder size (μm)	8.2		4.2	
Predicted pore radius for D ₁₀ (μm)	3.3	2.6	1.2	1.0
D ₅₀ powder size (μm)	15.9		10.3	
Predicted pore radius for D ₅₀ (μm)	6.4	5.1	2.9	2.4
D ₉₀ powder size (μm)	29.0		19.3	
Predicted pore radius for D ₉₀ (μm)	11.7	9.4	5.5	4.5
Measured maximum pore radius, r _p (μm)	7.3	5.2	4.4	4.1

List of figures

Fig. 1. Gas-atomized 316L stainless steel powder.

Fig. 2. Water-atomized 316L stainless steel powder.

Fig. 3. Porous microstructure of a sample made with 316L stainless steel water-atomized powder, 50 vol % powder loading sintered at 950°C.

Fig. 4. Porous microstructure of a sample made with 316L stainless steel gas-atomized powder, 50 vol % powder loading sintered at 950°C.

Fig. 5. Comparison between the calculated pore size radii using D_{10} , D_{50} , and D_{90} with the measured value for the DOE conditions 3, 4, 6, and 8.

Fig. 6. Thermal conductivity versus porosity as predicted by different models and as measured experimentally.

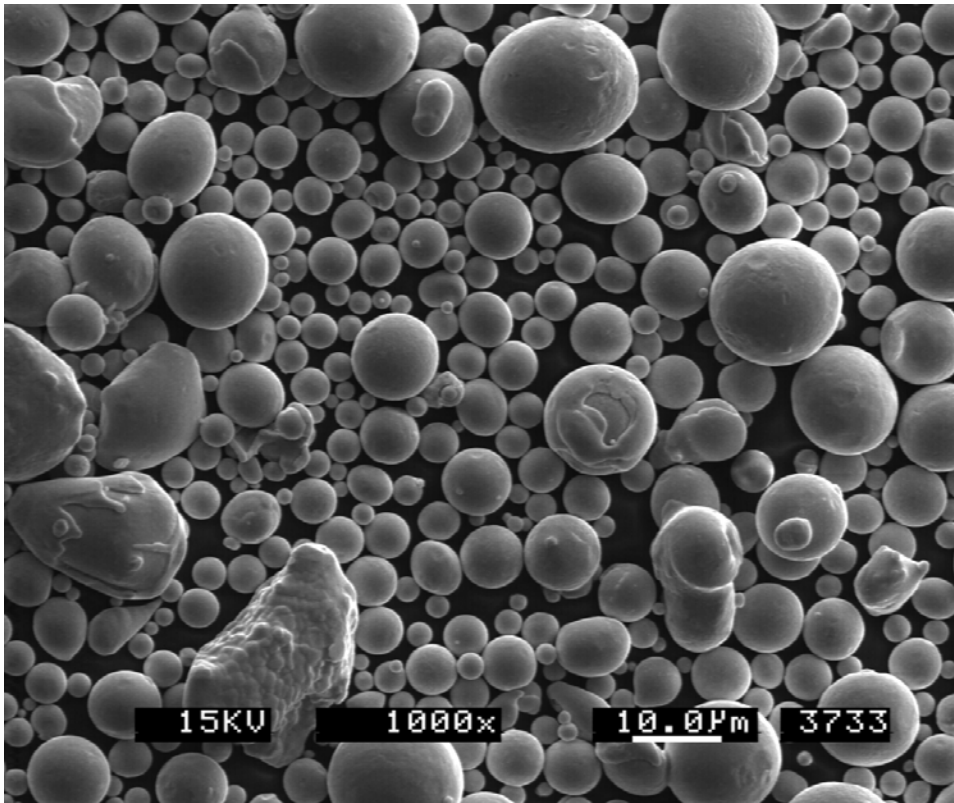


Fig. 1. Gas-atomized 316L stainless steel powder.

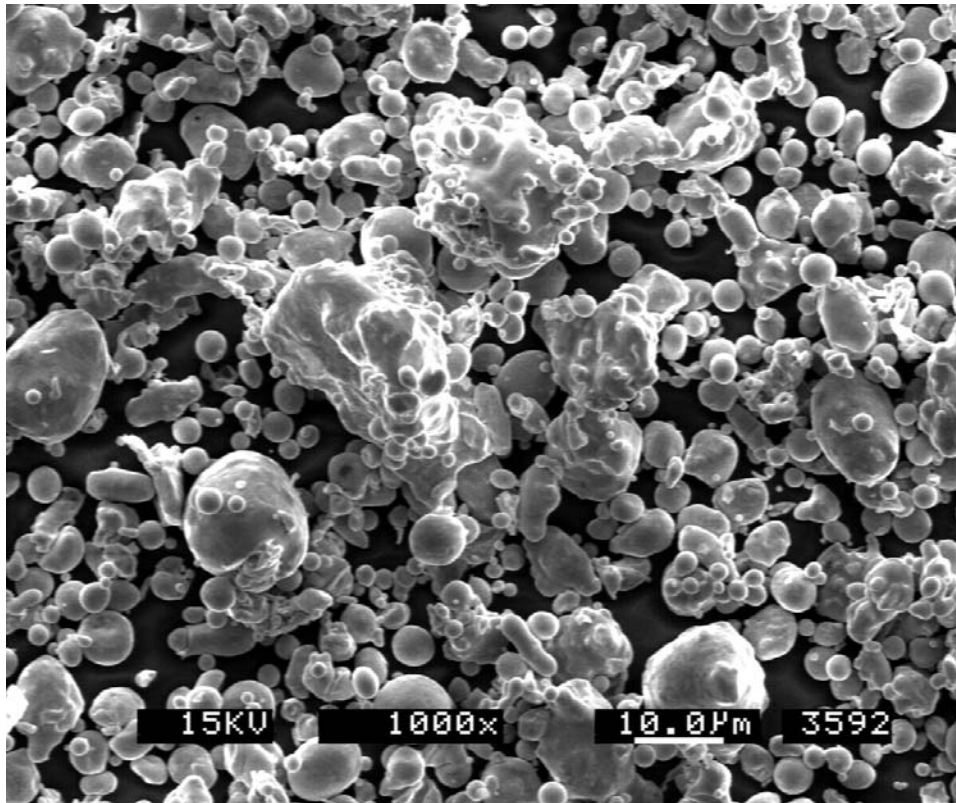


Fig. 2. Water-atomized 316L stainless steel powder.

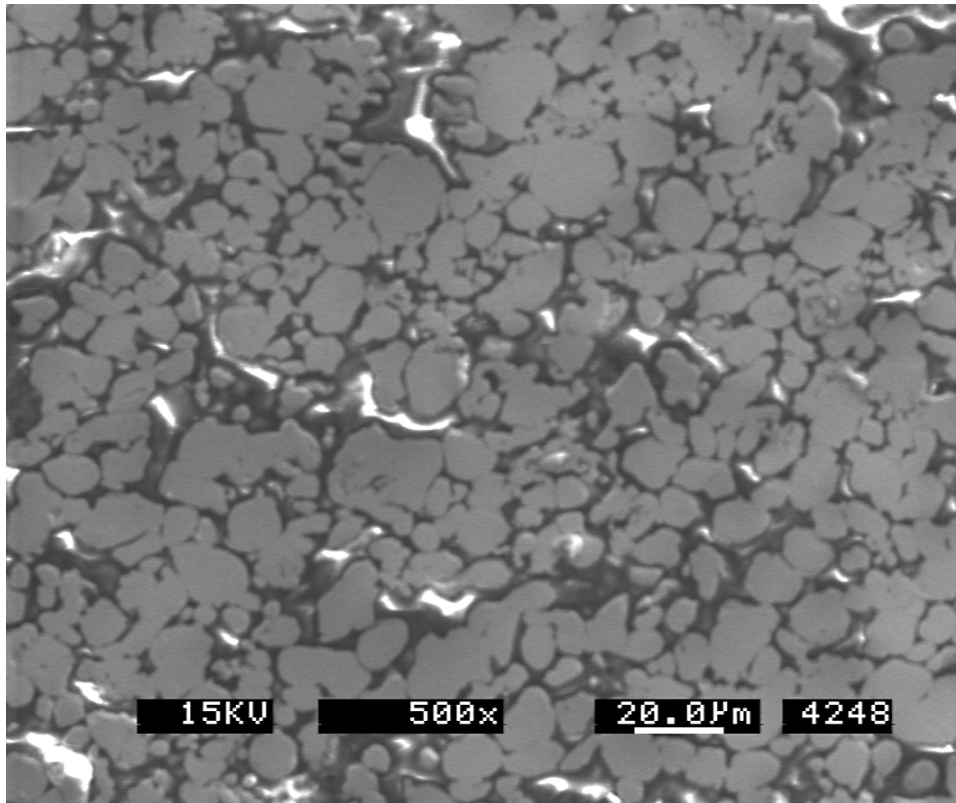


Fig. 3. Porous microstructure of a sample made with 316L stainless steel water-atomized powder, 50 vol % powder loading sintered at 950°C.

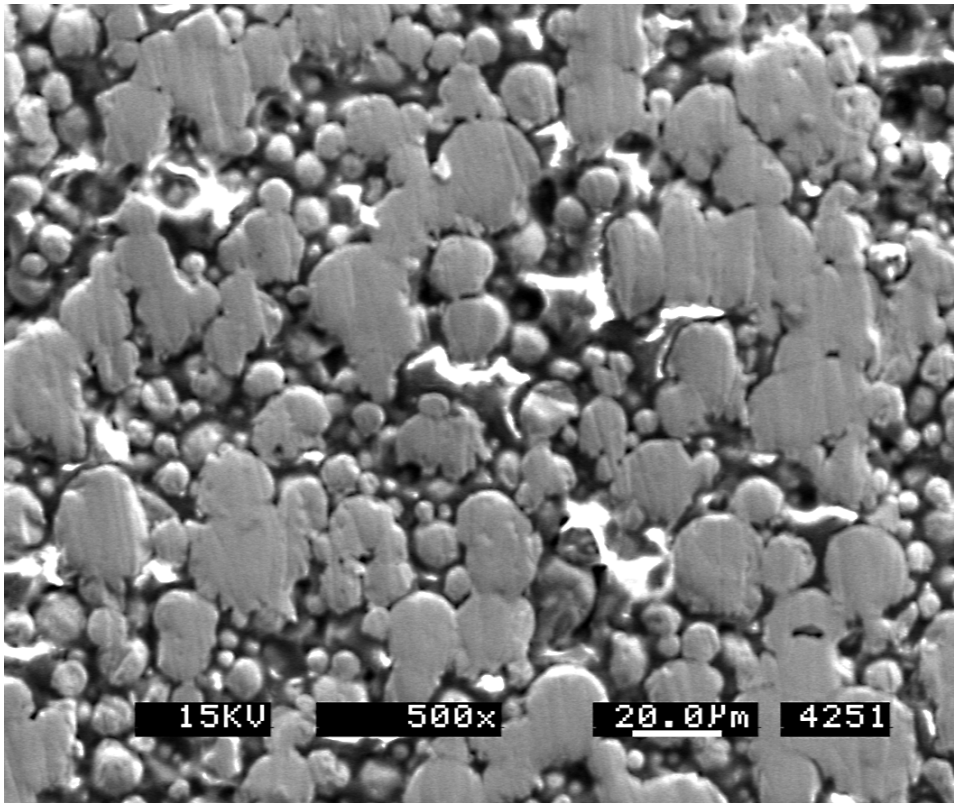


Fig. 4. Porous microstructure of a sample made with 316L stainless steel gas-atomized powder, 50 vol % powder loading sintered at 950°C.

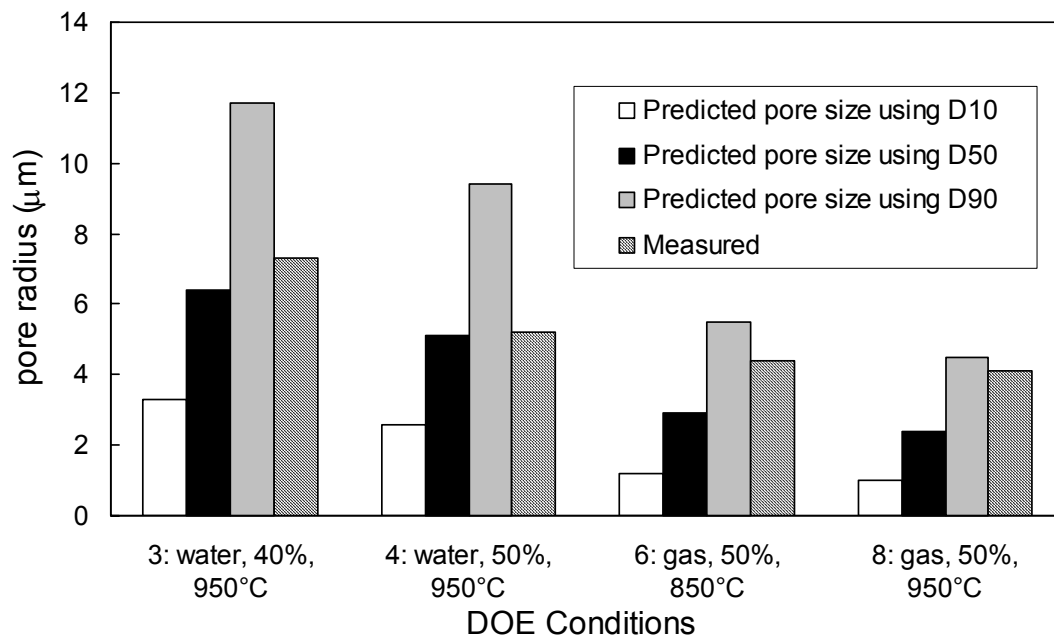


Fig. 5. Comparison between the calculated pore size radii using D_{10} , D_{50} , and D_{90} with the measured value for the DOE conditions 3, 4, 6, and 8.

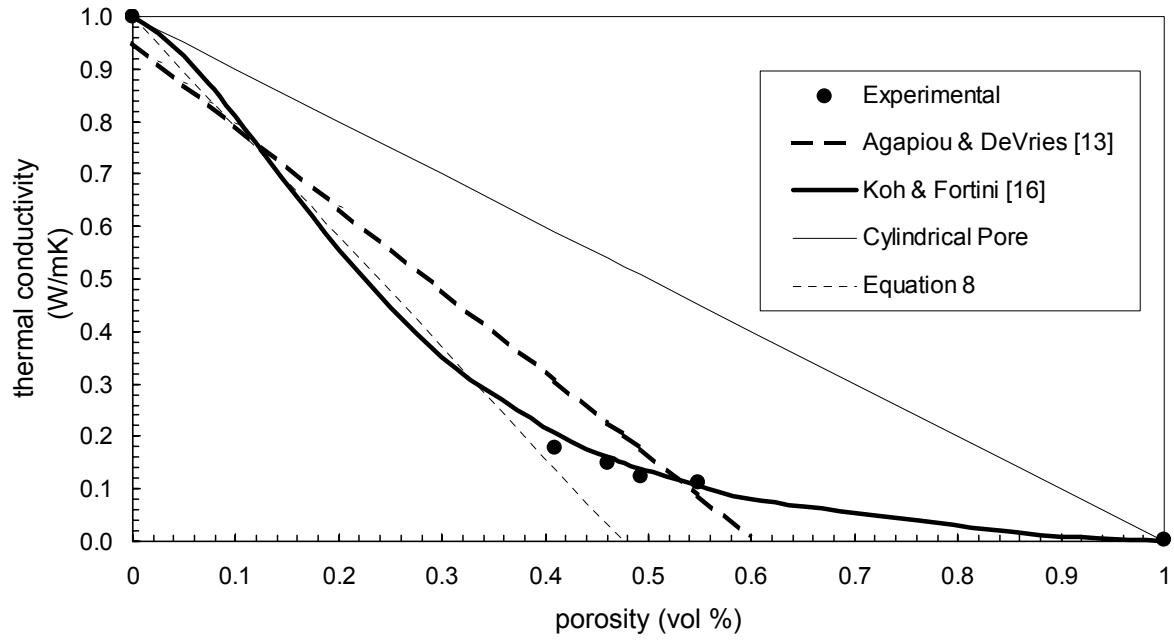


Fig. 6. Thermal conductivity versus porosity as predicted by different models and as measured experimentally.